FULL RESEARCH ARTICLE

Position-dependent mechanical characterization of the PBF-EB-manufactured Ti6Al4V alloy

Daniel Kotzem[1] · Alexandra Höffgen[1] · Rajevan Raveendran[1] · Felix Stern[1] · Kerstin Möhring[1] ·
Frank Walther[1]

Abstract

By means of additive manufacturing, the production of components with nearly unlimited geometrical design complexity is feasible. Especially, powder bed fusion techniques such as electron beam powder bed fusion (PBF-EB) are currently focused. However, equal material properties are mandatory to be able to transfer this technique to a wide scope of industrial applications. Within the scope of this work, the mechanical properties of the PBF-EB-manufactured Ti6Al4V alloy are investigated as a function of the position on the building platform. It can be stated that as-built surface roughness changes within building platform whereby highest surface roughness detected by computed tomography (Ra = 46.0 ± 5.3 μm) was found for specimens located in the front of the building platform. In contrast, no significant differences in relative density could be determined and specimens can be assumed as nearly fully dense (> 99.9%). Furthermore, all specimens are affected by an undersized effective diameter compared to the CAD data. Fatigue tests revealed that specimens in the front of the building platform show slightly lower performance at higher stress amplitudes as compared to specimens in the back of the building platform. However, process-induced notch-like defects based on the surface roughness were found to be the preferred location for early crack initiation.

Keywords Additive manufacturing · Electron beam powder bed fusion (PBF-EB) · Ti6Al4V · Fatigue properties

1 Introduction

As one of the most common used titanium alloys, Ti6Al4V is known for its good strength-to-weight and stiffness-to-weight ratio as well as other advantageous characteristics. Especially, the aerospace and automotive industry exploit the high specific strength of this alloy since significant weight savings are possible compared to Fe-based alloys. In comparison to other materials Ti6Al4V is also favored due to its good corrosion resistance and biocompatibility which is of great importance for medical implants [1–3]. However, the manufacturing of Ti6Al4V is still challenging and cost-intensive whereas new manufacturing techniques are needed to reduce the cost of production and the manufacturing period [1].

Additive manufacturing (AM) is known for its layer-by-layer manufacturing which enables a near-net-shape production. Powder bed fusion (PBF) is an AM technique (cf. ASTM F42 Committee [4]) based on a 3D-CAD model. During the manufacturing process, powder layers are deposited on a building plate and a high-energy source (laser or electron beam) fuses the powder bed by creating small melt pools. Subsequently, the process steps are repeated until the final part is built [1, 5]. Laser powder bed fusion (PBF-LB/M) manufactures parts in a chamber filled with inert gas [2]. However, electron beam powder bed fusion (PBF-EB) applies a high vacuum in the process chamber at increased processing temperatures (> 700 °C) [6, 7]. According to the possible process parameters, the PBF-EB process is particularly advantageous as it can result in reduced residual stresses [8] and minor contamination of other elements such as oxygen [2].

Until now, numerous studies regarding the microstructure, process-induced defects as well as the corresponding mechanical properties are available in literature (e.g., review articles [1, 9]). Typically, the PBF-EB-manufactured

✉ Daniel Kotzem
  daniel.kotzem@tu-dortmund.de

1   Chair of Materials Test Engineering (WPT), TU Dortmund University, Baroper Str. 303, 44227 Dortmund, Germany

Ti6Al4V alloy consists of a fine $\alpha + \beta$ microstructure [10, 11]. Thereby, specimens are often suffered by process-induced defects mainly resulting from non-optimal process parameters [12]. Two main types of defects are present which might be either gas pores or lack of fusion (LoF). These defects can partially be reduced when adjusting the process parameters. Facchini et al. [13] demonstrated that specimens with a relative density of 99.4% can be manufactured by means of PBF-EB. Later on, Elambasseril et al. [14] reported an even higher relative density (> 99.9%). Next to process-induced defects, even the increased surface roughness is challenging [15]. In detail, surface roughness values in the range of Ra = 24–41 μm were reported [16]. This irregular surface topography can support the formation of near-surface defects such as notch-like defects which can lead to stress concentrations negatively affecting the mechanical properties of the material. Within quasistatic tensile tests, it could be demonstrated that comparable mechanical strength as wrought Ti6Al4V (PBF-EB: YS = 830 MPa, UTS = 915 MPa [13]; Wrought: YS = 790 MPa, UTS = 870 MPa [13]) can be reached by the PBF-EB-manufactured material in machined condition [8, 13]. Within investigations done by Hrabe et al. [17] the effect of energy input on the quasistatic properties was examined. Thereby, it could be stated that yield stress (YS) and ultimate tensile strength (UTS) are only slightly reduced by 2–3% with decreasing energy input. Since many experimental data for Ti6Al4V in machined condition [11, 13, 14] are available, only few studies focus on the mechanical properties of Ti6Al4V with as-built surface roughness. Solely, Koike et al. [18] reported a yield stress YS = 720 MPa and ultimate tensile strength UTS = 780 MPa for PBF-EB-manufactured Ti6Al4V with as-built surface roughness.

Predicting the fatigue behavior PBF-EB Ti6Al4V is even more challenging although process parameters have been improved in the last years. In a recent study, Chern et al. [9] compared and discussed the effect of build orientation, surface roughness and hot isostatic pressing (HIP) on the fatigue properties of PBF-EB-manufactured Ti6Al4V. Thereby, it was stated that up to 100 different process parameters such as quality of the initial powder, focus and line offset, energy input, scanning strategy and location on the building platform (BP) can affect the fatigue life of AM components. Especially for Ti6Al4V, it was shown that an anisotropic material behavior is observed for as-built material with initial surface roughness, whereby horizontal manufactured specimens show superior fatigue performance compared to vertical ones. After machining, the effects of build orientation are negligible. An additional thermal treatment such as annealing or stress relief heat treatment was found to have nearly no influence on PBF-EB-manufactured Ti6Al4V. The best fatigue performance was achieved when both machining and HIP were carried out. However, HIPed specimens with as-built surface roughness did not show a significant difference to material in as-built condition. [9]

In order to enhance the fatigue performance of PBF-EB-manufactured components with a more complex shape, conventional machining is difficult whereas additional treatments are needed. Persenot et al. [19] demonstrated that chemical etching can smooth the specimen's surface and, thus, improves the fatigue behavior. Tomographic scans showed that the crack initiation in low cycle fatigue (LCF) mainly initiated at a near-surface notch defect. However, remaining internal defects still have a huge impact on the fatigue behavior so that a combination of HIP and chemical etching was applied. Thereby, authors examined a significant enhancement in fatigue performance due to decreased surface roughness and nearly fully dense specimens with partial reduction of near-surface notch defects resulting in an improved fatigue strength for PBF-EB-manufactured Ti6Al4V. Although a lot research was carried out investigating the fatigue properties of Ti6Al4V, only few studies consider the individual process-induced properties of each specimen within one build job as a function of the position on the BP. Gallaraga et al. [20] investigated the influence of different locations on the BP by means of quasistatic tensile tests. It was reported that specimens in the front of the BP showed highest values of YS and UTS. Lowest values of YS and UTS were determined for specimens in the center of the BP.

Within this work, the PBF-EB-manufactured Ti6Al4V alloy is characterized by optical metallography, scanning electron microscopy (SEM), X-ray diffractometry (XRD), defect distribution and hardness measurements as a function of the specimens' position on the BP. Subsequently, the influence of process-induced irregularities on the mechanical behavior is investigated by means of fatigue tests to enable a better insight into the process–structure–property relationship of PBF-EB-manufactured Ti6Al4V.

2 Experimental procedure

The investigated Ti6Al4V alloy was processed by PBF-EB on an Arcam A2X (Arcam AB, Mölndal, Sweden). A standard melting scheme for Ti6Al4V was used for manufacturing the specimens upright following five repetitive steps during each cycle: (1) the defocused electron beam preheats the chamber and the individual powder layers, (2) the focused electron beam melts the layer by contouring, (3) hatching according to the CAD geometry, (4) fabricated layers are post-heated and (5) a new powder layer is placed on the previous deposited one while the platform is lowered down. The BP was divided into 30 equal areas and the specimens were separately numbered. Within this study, all specimens with even numbers were considered having a gauge diameter of

3 mm (Fig. 1c). A detailed figure regarding the segregation of the BP can be seen in Fig. 1a, b.

Surface roughness was examined along building direction (BD) using a surface roughness tester M 300 C (Mahr Gruppe, Göttingen, Germany). Hardness measurements (HV 0.2) were carried out with a micro hardness tester HMV-G-FA (Shimadzu, Kyoto, Japan) and accomplished on the upper part of every specimen (directly above gauge length) to avoid any impact for posterior fatigue testing. Five hardness measurements were performed and averaged according to ISO 6507.

For microstructural investigations, a slice of 2 mm thickness was extracted from exemplary specimens at similar position as hardness measurements were carried out. The slices were electrically embedded, ground (320–4000 grit) and subsequently polished with oxide polishing suspension (OP-S). Light microscope investigations were performed on the light microscope Axio Imager (Carl Zeiss, Oberkochen, Germany). Therefore, samples were etched (78 ml distilled water, 12 ml 40 wt% potassium hydroxide solution, 15 ml 30 wt% hydrogen peroxide solution) for 10–40 s. Additional qualitative phase analysis was conducted using X-ray diffractometry. Therefore, the X-ray diffractometer (XRD) D8 Discover (Bruker, Billerica, MA, USA) with a Cu-Kα radiation source was used. With regard to process-induced defect distribution, every sample was investigated by X-ray microfocus computed tomography (μ-CT) using the system XT-H 160 (Nikon Metrology, Tokyo, Japan). The maximum acceleration capacity is 160 kV generating a micro-focus of 3 μm. The used scanning parameters are listed in Table 1. 2D pore analysis was carried out for every scanned specimen. Therefore, the reconstructed volumes were sliced into at least 100 images along BD. Subsequently, the image processing program ImageJ was used to binarize the images. Deviations between the initial CAD diameter and the real contour were determined and averaged for the examined samples. The average cross section and equivalent diameter of every investigated specimen was used as a basis for the later mechanical testing. With regard to the increased as-built surface roughness, the results from μ-CT were also used to determine the surface roughness. Therefore, surface profiles were extracted from a radial slice every 10° around the symmetry axis. Further information regarding the evaluation methods can be found in [21].

With the intention to evaluate the mechanical properties, fatigue tests were carried out on the servohydraulic testing system Schenck PC63M (Instron®, Norwood, USA) with an Instron 8800 controller. In particular, constant amplitude tests (CAT) were performed under tension–compression loading ($R = -1$) using a test frequency of $f = 5$ Hz. For the as-built specimens, six different stress amplitudes were selected. Detailed information regarding the chosen stress amplitudes can be seen in Table 2. On each stress amplitude, at least two specimens were tested. The fractographic
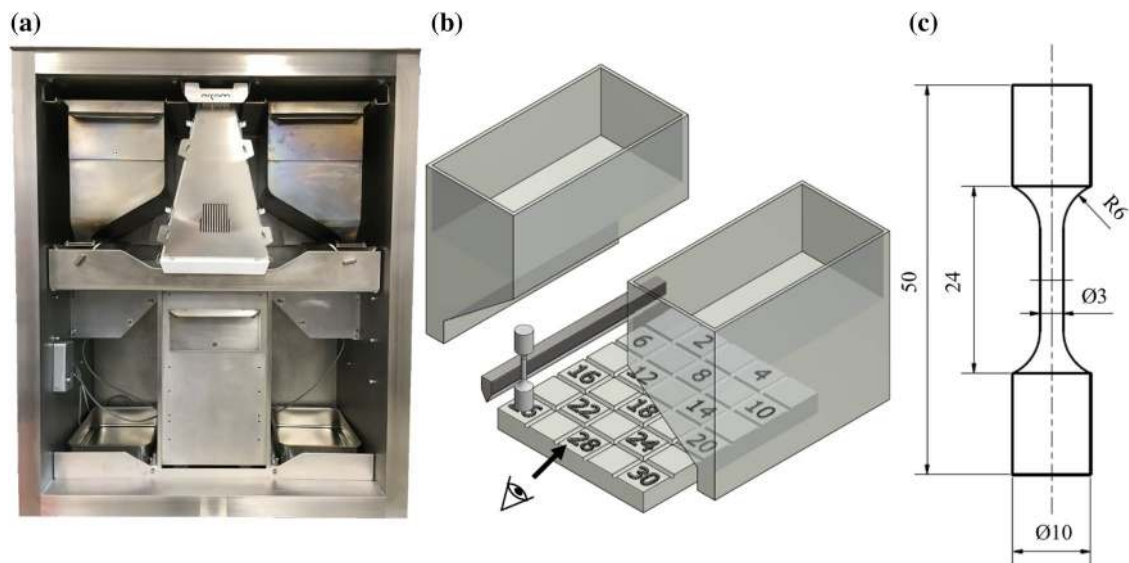

Fig. 1 **a** Arcam EBM A2X, **b** schematic illustration of segmentation of build platform and **c** the specimen geometry used for fatigue testing (dimensions in mm)

Table 1 Scanning parameters for the computed tomography scans (μ-CT)

	Material	Beam energy	Beam current	Power	Effective pixel size	Exposure rates
	Ti6Al4V	149 kV	60 μA	8.94 W	7 μm	354 ms	2.82 fps

Table 2 Selected stress amplitudes for the constant amplitude tests (CAT)

Material condition	Stress amplitudes σ_a [MPa]
As-built	180, 210, 240, 270, 300, 330

analysis was carried out on a SEM Mira 3 XMU (Tescan, Brno, Czech Republic).

3 Results

3.1 Surface roughness

The results from surface roughness measurements are shown in Fig. 2a, b. Specimen 1 is located in the upper left corner and specimen 30 is located in the bottom right corner, respectively (cf. Fig. 1b). As already mentioned in Sect. 2, two different measuring techniques, i.e., tactile surface roughness tester and μ-CT were used. The average surface roughness value for all investigated specimens which were tested with tactile surface roughness tester was found to be Ra = 20.9 ± 1.3 μm whereby Fig. 2a shows the arrangement of all specimens on the BP with their associated Ra value. All values range between the least surface roughness of specimen 24 amounting Ra = 18.4 μm and specimen 18 having a value of Ra = 23.3 μm. Regular trends of occurring roughness values on the BP were not observed. Taking into account the Ra values from μ-CT, it can be seen, that the results differ significantly with respect to the measurement technique. In general, calculated Ra values from μ-CT are nearly twice as high as Ra values which were measured by tactile surface roughness tester and average surface roughness was found to be Ra = 40.7 ± 2.3 μm. Furthermore, it can be mentioned that specimens in the front of the BP show higher Ra values, especially specimen 26 with a maximum Ra = 46.0 ± 5.3 μm, compared to the back of the BP.

3.2 Initial hardness

Hardness measurements were conducted for all investigated specimens and averaged overall hardness was found to be 331 ± 10 HV. Figure 3 represents the hardness values as a function of the position on the BP. As can be seen, hardness values are distributed heterogeneously over the entire BP. In particular, the specimen with highest hardness (specimen 18) is closely located to the specimen with lowest hardness (specimen 12). All values range between 312 and 351 HV.

	323 ± 3 HV		328 ± 1 HV	
341 ± 3 HV		324 ± 3 HV		336 ± 3 HV
	312 ± 1 HV		332 ± 6 HV	
334 ± 3 HV		351 ± 2 HV		332 ± 3 HV
	327 ± 10 HV		332 ± 3 HV	
339 ± 6 HV		315 ± 4 HV		335 ± 7 HV

Fig. 3 Hardness values in accordance to the positions on the building platform

Fig. 2 Surface roughness values Ra in μm measured with **a** tactile surface roughness tester and **b** μ-CT in accommodation to the positions on the building platform. Specimen 1 is located in the upper left corner and specimen 30 is located in the bottom right corner, respectively

(a)

	19.0 ± 2.2 μm		20.0 ± 1.0 μm	
22.5 ± 2.2 μm		21.0 ± 1.5 μm		20.8 ± 1.6 μm
	21.5 ± 0.7 μm		22.3 ± 1.7 μm	
20.6 ± 1.4 μm		23.3 ± 0.8 μm		21.7 ± 1.2 μm
	19.7 ± 3.3 μm		18.4 ± 1.5 μm	
21.6 ± 2.1 μm		21.3 ± 0.9 μm		20.3 ± 2.7 μm

(b)

	38.4 ± 3.8 μm		38.8 ± 3.7 μm	
38.9 ± 5.0 μm		39.0 ± 3.7 μm		40.0 ± 4.4 μm
	39.6 ± 4.5 μm		39.1 ± 4.7 μm	
39.4 ± 4.6 μm		40.8 ± 4.4 μm		39.2 ± 3.7 μm
	45.3 ± 10.3 μm		42.8 ± 5.0 μm	
46.0 ± 5.3 μm		41.3 ± 5.3 μm		42.0 ± 4.1 μm

3.3 Process-induced microstructure, defect distribution and geometrical accuracy

Based on the results from hardness measurements, the specimen with lowest (specimen 12) and highest (specimen 18) hardness were subsequently used for microstructural investigations. Thereby, a fine $\alpha + \beta$ microstructure was detected which is comparable to other studies [1, 2]. Zhai et al. [11] stated that this structure develops due to the increased manufacturing temperatures as well as the slow cool down after finishing the build job. However, taking into account the light microscope images for both specimens, no significant differences between the specimens with lowest and highest hardness are discernible assuming that the microstructure is similar for all specimens.

In order to verify the existence of the β phase, additional XRD analysis was carried out. Figure 4 shows the XRD pattern for the PBF-EB-manufactured Ti6Al4V alloy whereby the majority of the peaks can be attributed to the α/α' phase. Since α and α' have the same hexagonal close-packed (hcp) structure, a clear differentiation between both phases is challenging [10]. However, it was already reported in [1, 11] that the α' phase can be completely eliminated during the PBF-EB process. Next to the α/α' phase, even the body centered cubic (bcc) β phase is present (cf. Fig. 5), which was earlier reported by different researchers [13, 22].

As mentioned above, pore analysis was carried out based on 2D images which were extracted from the reconstructed μ-CT volumes. Taking into account the complete BP, it can be stated that no big differences or regularly appearing deviations in relative density are present (cf. Fig. 5a). Smallest relative density was found to be 99.92% for specimen 10. However, specimens in direct vicinity (e.g., specimen 8, 14, 20) even show highest relative density. Since all values
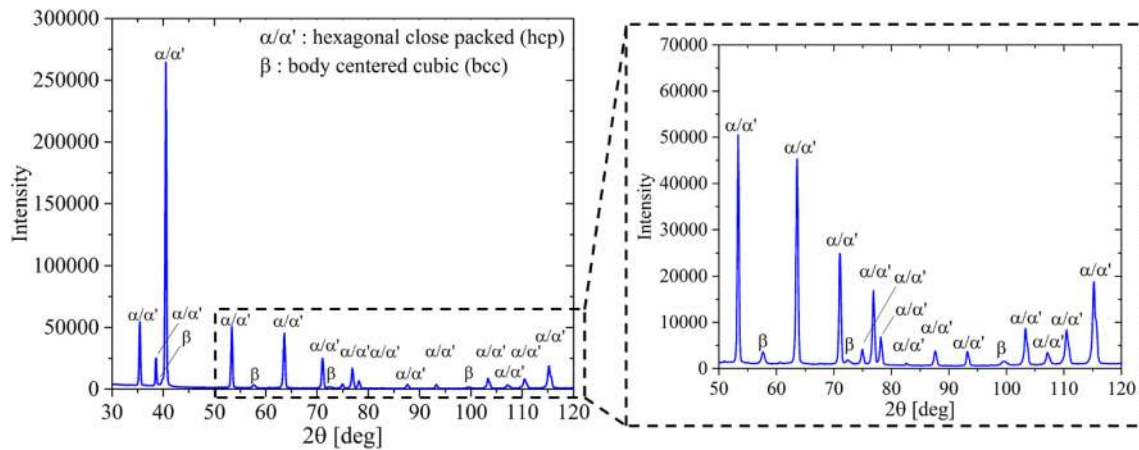

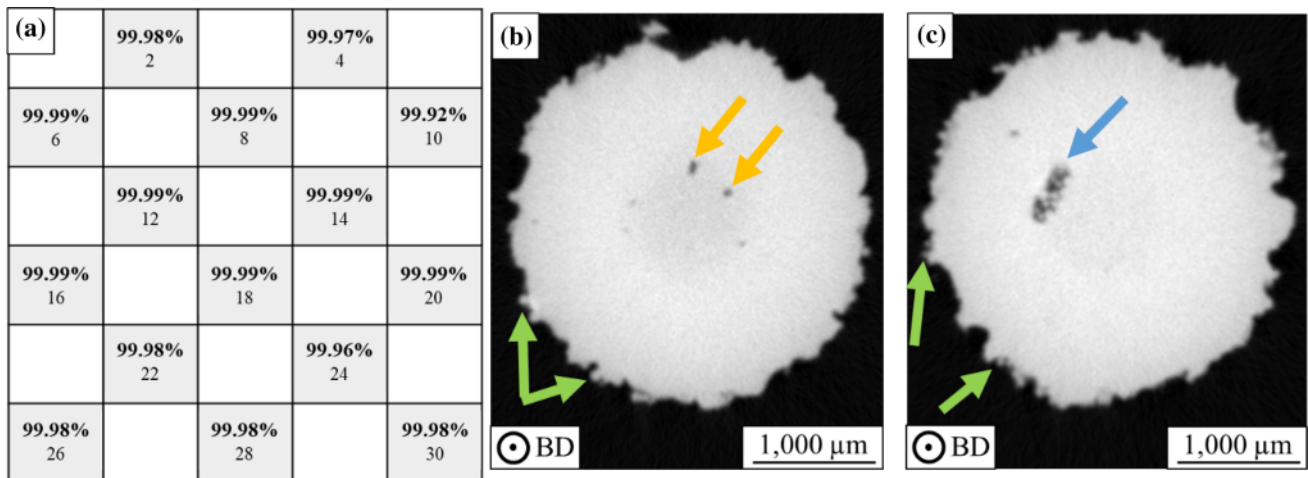**Fig. 4** XRD patterns of PBF-EB-manufactured Ti6Al4V alloy

Fig. 5 **a** Values for relative density according to the positions on the building platform and 2D CT images from cross sections of specimen 10 showing predominantly **b** gas pores and **c** lack of fusion (LoF)

only show differences in the second decimal place, it can be assumed that near fully dense specimens were manufactured. The remaining defects can be differentiated in two main pore types which can influence the fatigue behavior. The majority of all found pores are spherical shaped which is typical for gas pores having a diameter of approx. 20 μm. These circular pores are exemplarily shown in Fig. 5b (marked with orange arrows). In comparison, only a few elongated shaped and relatively larger LoF pores were detected. An exemplary LoF defect is highlighted by a blue arrow in Fig. 5c whereby a few unmolten powder particles can be observed inside the LoF defect. Furthermore, the combination of surface roughness, waviness and inaccuracy of the geometrical shape can be seen in the contour region in Fig. 5b, c, respectively. Green arrows exemplarily point out partially melted powder particles sticking on the specimens' surface.

PBF-EB-manufactured specimens can suffer from geometrical deviations when compared to the initial CAD data [19, 23]. Furthermore, these deviations can locally change with regard to the position on the BP. Therefore, average equivalent diameter was calculated for all specimens based on the μ-CT scans. The local differences between CAD and average equivalent diameter are plotted in Fig. 6a. In general, it can be stated that all sample cross sections are smaller than the prescribed CAD cross section and average deviation was found to be $-5.34 \pm 0.50\%$. In detail, specimen 20 showed the lowest deviation of -4.16% corresponding to the largest equivalent diameter which was found to be 2.88 mm. Highest deviation, in total -6.23%, was found for specimen 18 resulting in the smallest average cross section. The actual diameter for specimen 18 within the investigated gauge length is presented in Fig. 6b and is colored in black. The average equivalent diameter of 2.81 mm is marked in

red color and the CAD diameter of 3 mm is presented in blue, respectively. As can be seen, actual specimen diameter changes between single material layers which might lead to the formation of notch-like defects. Notch-like defects are typically described by their geometrical parameters such as depth and thickness of the notch as well as the radius at the lowest point [24]. The total amplitude of local diameter deviations ranges between 2.78 and 2.85 mm.

3.4 Mechanical properties

The basis for the following fatigue tests are the calculated values for the average equivalent diameter which were introduced above. The fatigue tests were performed at different stress amplitudes to investigate the material's cyclic properties. The results are given in Fig. 7.
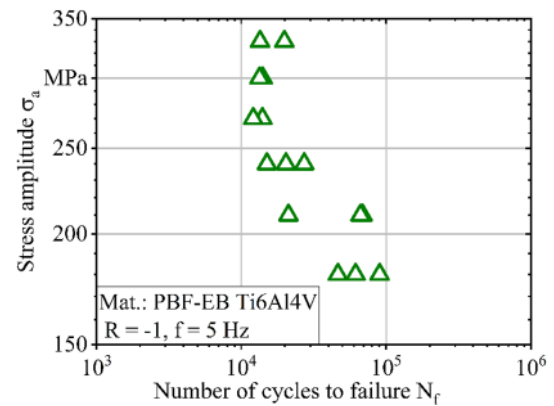
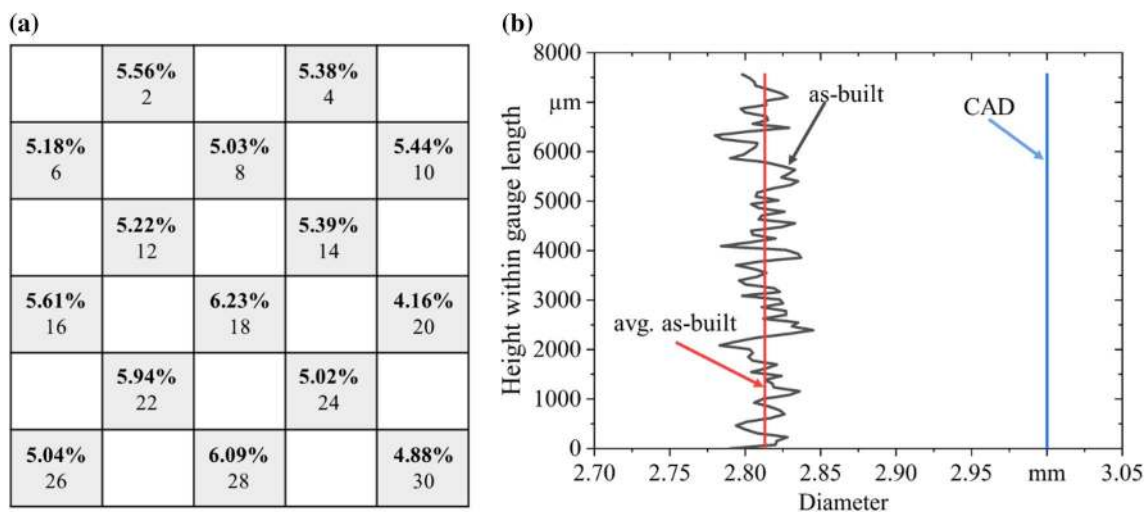**Fig. 7** Results from CAT plotted in form of S–N curves

Fig. 6 **a** Local differences on building platform between CAD- and average equivalent diameter in percent in accordance with platform number. **b** Graphic depiction of cross section variations, average diameter and CAD diameter along building direction for specimen 18
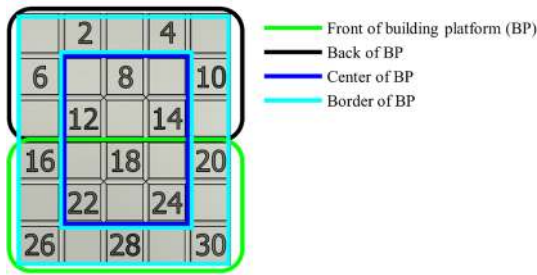
Fig. 8 Segmentation of the building platform

As can be seen, fatigue life values of as-built specimens are ranging between 10^4 and 10^5 cycles. For a stress amplitude $\sigma_a = 180$ MPa, a maximum number of cycles to failure $N_f = 90,200$ cycles was detected. However, for stress amplitudes ranging between 240 and 330 MPa, comparable number of cycles to failure were determined.

Furthermore, it can be seen that fatigue life of the as-built samples scatter more at lower stress levels, especially at a

stress amplitude $\sigma_a = 210$ MPa. To further investigate the influence of the position of the BP on the fatigue life, the BP was divided into either front and back or center and border areas, as can be seen in Fig. 8.

Based on this segmentation, specimens of each area were separately colored and results are plotted in Fig. 9a, b. In detail, specimens in the front of the BP are colored in light green, in the back of the BP in black, in the center of the BP in blue and in the border of the BP in light blue. Taking into account the results plotted, no clear influence of the position on the BP is visible. However, it has to be mentioned that specimens in the front of the BP show slightly weaker fatigue performance at higher stress amplitudes (cf. Fig. 9a). With decreasing stress amplitude, differences are reduced. Even specimens positioned at the border of the BP show lower fatigue life compared to specimens located in the center of BP (cf. Fig. 9b). This phenomenon can be detected at higher as well as at lower stress amplitudes. Solely specimen 14 ($\sigma_a = 210$ MPa, $N_f = 21,188$ cycles) shows a contrary tendency implicating that an individual irregularity led to

Fig. 9 Results from CAT plotted in form of S–N curves: differentiation between **a** front and back and **b** center and border of the BP
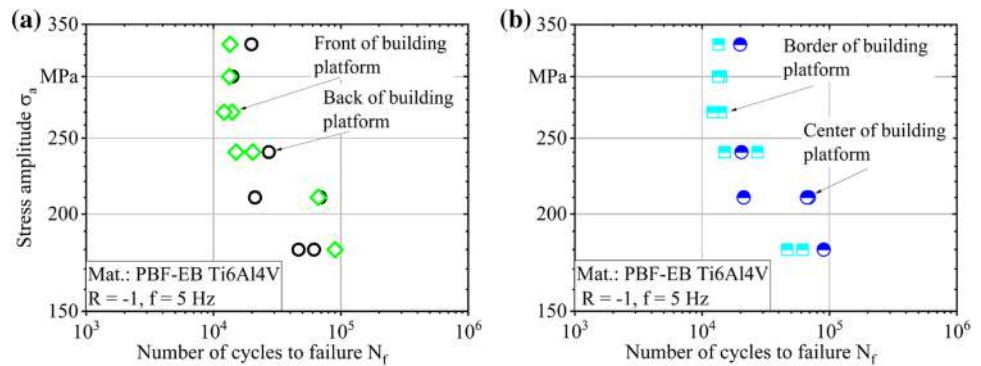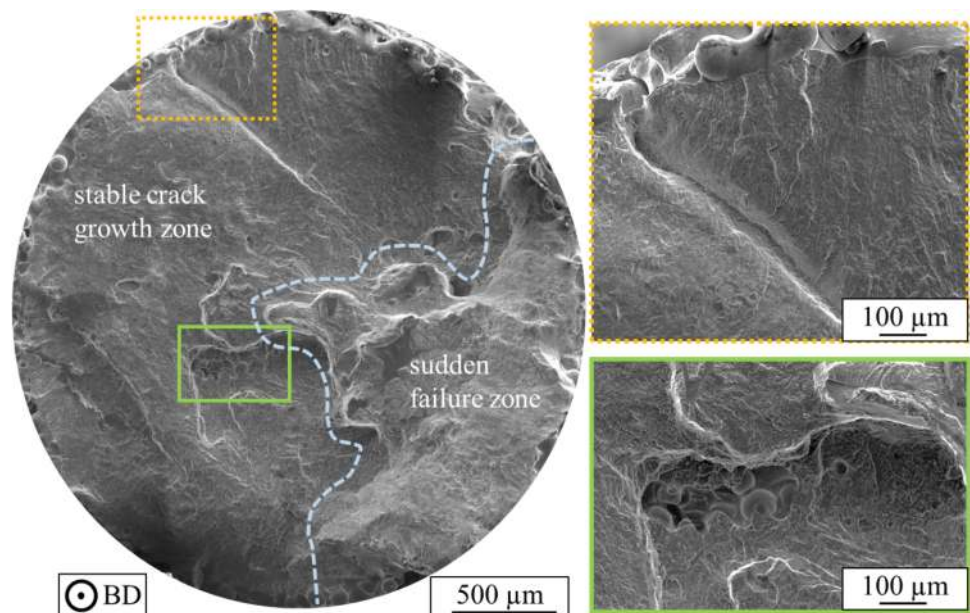

Fig. 10 Fracture surface of specimen 10 tested at a stress amplitude of $\sigma_a = 240$ MPa ($N_f = 27,210$ cycles)

early failure. Nevertheless, further investigations considering an increased number of specimens are needed to clearly confirm these findings.

3.5 Fractographic analysis

The fractured surface of specimen 10 ($\sigma_a = 240$ MPa, $N_f = 27{,}210$ cycles), representing a specimen from the front of BP, was subsequently analyzed to localize the initiation of the fracture and to retrace crack growth mechanisms. The fractographic image as well as two magnifications are plotted in Fig. 10. As can be seen, the fatigue crack originated at the specimen surface which can mainly be attributed to the increased as-built surface roughness and near-surface defects leading to an irregular surface topography. However, based on the interaction of multiple factors, the fracture initiation cannot be attributed to a single origin. Furthermore, the fractured surface can be subdivided into two areas which are separated by a dashed line colored in light gray.

On the left side, the stable crack growth zone is clearly visible which is typically relatively flat and even. Within the stable crack growth zone, small spherical pores and certain LoF can be observed which are shown in higher magnification. Next to the stable crack growth zone, the second area shows a sharp und uneven surface which is characteristic for the sudden failure zone. In this zone, the specimen failure is caused by an overload fracture.

For comparison, the fractured surface of specimen 14 ($\sigma_a = 210$ MPa, $N_f = 21{,}188$ cycles) is shown in Fig. 11. This specimen is located in the back of BP and showed relatively low fatigue life during CAT. As can be seen, even here, multiple crack initiation sites are present and fatigue crack initiated at the surface.

Additionally, process-induced defects are visible within the stable crack growth zone. However, no local characteristics are visible on the fractured surface implicating that a combination of surface defects and roughness results in an irregular surface topography which leads to early failure under cyclic loading.

4 Discussion

4.1 Surface roughness

PBF-EB-manufactured as-built components clearly show an increased surface roughness compared to machined ones, as can be seen in Fig. 2a, b. In this study, the average roughness value determined with tactile surface roughness tester was found to be Ra = 20.9 ± 1.3 μm. For comparison, additional surface roughness determination was conducted based on the reconstructed μ-CT volumes which was earlier introduced by Persenot et al. [19]. Thereby, Ra values are nearly doubled. In general, process parameters can affect the occurrence and formation of layer defects or lead to partially melted powder particles sticking on the specimens' surface [25]. As highlighted in Fig. 6b, the surface profile which was determined by μ-CT shows an irregular topography consisting of several peaks and valleys. Since valleys are deep and sharp-etched, the tactile measuring needle could not fully capture the present surface profile which might explain the significant differences between the two measuring techniques.

Wang et al. [16] investigated the effect of different processing parameters on the as-built surface roughness of PBF-EB Ti6Al4V whereby surface roughness was determined by tactile surface roughness tester. The best

Fig. 11 Fracture surface of specimen 14 tested at a stress amplitude of $\sigma_a = 210$ MPa ($N_f = 21{,}188$ cycles)
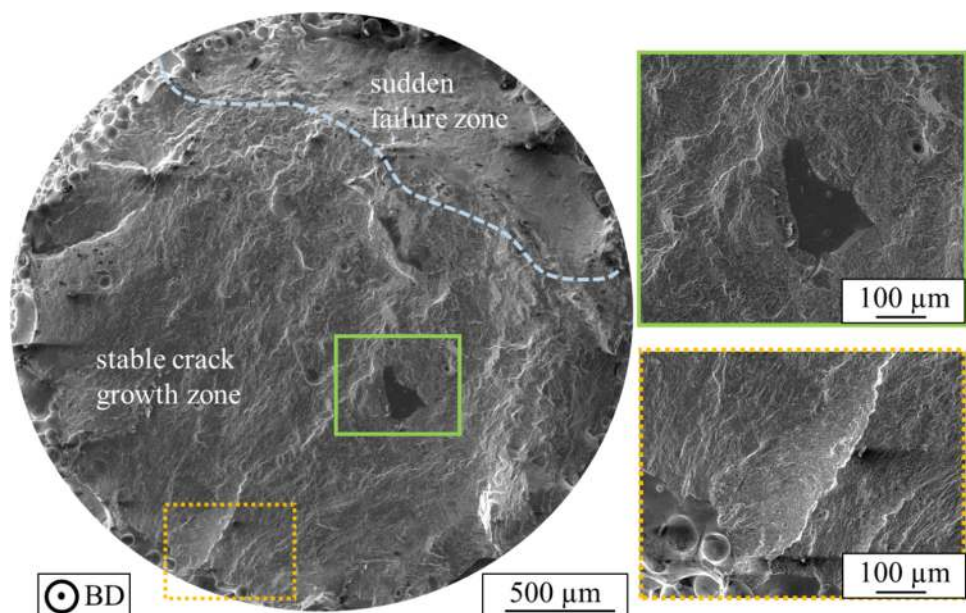
parameter setting in terms of reducing surface roughness resulted in a surface roughness value Ra = 24 µm which is in accordance with the roughness values examined in this study. In contrast to this, Persenot et al. [26] determined a higher surface roughness Ra = 44 µm for PBF-EB-manufactured Ti6Al4V as-built specimens which is comparable to the results presented when µ-CT results are considered. However, it can be clearly seen that surface roughness determination is still challenging and further investigations and standardized methods are needed. Generally, the interaction of several factors impact the surface quality resulting in higher roughness for PBF-EB-manufactured components whereby Persenot et al. [26] mainly attributed the process-induced surface roughness to the partially melted powder particles, which are sticking to the surface, as well as "plate-pile" like stacking defects. Suard et al. [27] and Körner et al. [28] observed "plate-pile" like stacking defects as a result of the flexibility of the electron beam. Thereby, individual layers are not melted precisely (convex or concave shape) resulting in the formation of notch-like defects at the surface. According to Li et al. [2], variations on surfaces and overhangs occur even under nearly optimal process parameters. Influential parameters were found to be the speed function, layer thickness and powder particle size. Especially powder particle characteristics, e.g., particle size and shape, influence the surface roughness directly. Furthermore, the thermal behavior, relative density and energy absorption depend on powder characteristics resulting in variations during the manufacturing process [2]. Suard et al. [27] have shown in their investigations that the thermal behavior can also impact surface irregularities. Upright manufactured specimens show relatively homogenous roughness over the entire specimen height due to mainly constant thermal flux through the strut during processing. This constant thermal flux favors the equiaxed shape of the specimens; however, high beam energy causes thermal radiation leading to the formation of partially melted powder particles covering the whole surface [1]. Figure 2a, b shows comparative results and low standard deviations were determined for the Ra values implicating homogenous surface roughness for every single specimen. However, as a consequence of all possible types of surface irregularities the formation of an individual surface topography consisting of sharp edges and notch-like defects is favored which might explain the local differences of surface roughness over the entire BP (cf. Fig. 2a, b). Since these irregularities cannot be completely prevented, post treatments to smoothen the surface are often carried out. In order to increase the fatigue performance, chemical etching or conventional machining in combination with HIP was accomplished in previous studies [1, 2, 29].

4.2 Initial hardness

Hardness measurements for all specimens were found to be 331 ± 10 HV on average. As displayed in Fig. 3, hardness values over the entire BP does not show significant differences and regular deviations were not observed. Within investigations done by Masuo et al. [6] an average hardness of 369 HV for PBF-EB-manufactured specimens was determined, which is slightly higher than the results presented in this study. The absence of harder martensitic structures is characteristic for the PBF-EB-manufactured Ti6Al4V alloy and results in lower hardness values compared to other AM techniques such as PBF-LB/M. According to Dallago et al. [30], average hardness for PBF-LB/M manufactured specimens was found to be 380 HV resulting from several martensitic areas. Hardness values in this study are accordingly lower due to the process- and geometric-related lower cooling rates and the predominant α-phase morphology (cf. Fig. 4).

4.3 Process-induced microstructure, defect distribution and geometrical accuracy

Typically, the PBF-EB-manufactured Ti6Al4V alloy consists of a fine $\alpha + \beta$ microstructure [10, 11]. Thereby, it was already stated that the α' martensitic phase can be completely decomposed within the PBF-EB process due to the high processing temperatures whereby the as-built state can be considered as annealed condition [31]. According to Liu et al. [1], hardness corresponds to microstructure, which can be predicted by precise temperature and cooling rate data. However, no significant differences within the microstructural investigations were found for specimens having the highest and the lowest hardness. Based on the XRD analysis (cf. Fig. 4), the presence of the β phase could be determined. Similar results were earlier reported by Facchini et al. [13] and Ataee et al. [32] showing that most of the peaks within the XRD analysis can be attributed to the hexagonal close-packed titanium (hcp-Ti) and only low amounts of the β phase are present in the as-built condition.

As already stated in the introduction, the PBF-EB process enables the production of almost fully dense material [13, 14]. Based on the results, the average relative density of all investigated specimens was found to be > 99.9% whereby spherical shaped pores (cf. Fig. 5b) appeared more often than LoF defects (cf. Fig. 5c). Furthermore, pores occurred randomly within the volume and no pattern is visible. Similar results were even reported by Persenot et al. [24]. Typically, spherical pores can be attributed to entrapped gas in the powder particles. Varying the process parameters such as decreasing the scan speed and increasing the beam power can slightly prevent the development of gas pores, however, due to preexisting gas within the powder particles, gas pores

can hardly be eliminated [1, 27]. According to Li et al. [2], larger and non-spherical pores can reduce the fatigue performance significantly whereas the impact on the fatigue life of spherical defects was found to have minor influence. Those pores which are detrimental in terms of the fatigue performance occur due to an instability of the process parameters or inaccurate powder layer distribution [2]. Another factor for non-specific shaped pores might be also micro shrinkages during the process [26].

For manufacturing the Ti6Al4V specimens, the default Arcam process parameters for this titanium alloy were used. Within this study, all investigated specimens are systematically smaller than dictated by the CAD model, resulting in an undersized effective diameter. Within investigations done by Persenot et al. [26], a difference between CAD and average cross section of -13% for upright manufactured as-built specimens was detected. With regard to Fig. 6a, slightly lower deviations, ranging around $-5.34 \pm 0.50\%$, were determined. Vo et al. [33] demonstrated that different process parameters such as offset and speed function can influence the geometric accuracy especially the loss of thickness due to overheating. Taking into account the geometrical shape of the specimens within gauge length, a relative round shape is visible. Suard et al. [27] have reported that next to vertical even oblique oriented struts show a rather equiaxed shape. The authors justify the uniaxial cross section shape of their specimens with a different thermal conductivity of the sintered powder and the bulk material. Due to a higher thermal conductivity of the bulk, thermal flux dissipates more often equally through the molten pool than the powder. It can be seen that optimal process parameters result in a better accuracy and lower geometrical deviations compared to the CAD model [27]. The reduction of the effective diameter for upright manufactured specimens is of minor importance; however, it should be considered in terms of dimensioning of components in the near-net-shape production, as there are deviations before any post-treatment.

4.4 Mechanical properties and fractographic analysis

Taking into account the PBF-EB-manufactured Ti6Al4V alloy in machined condition, comparable or even enhanced fatigue properties as for conventional manufactured material can be achieved [9]. However, as stated by Kahlin et al. [34], as-built surface roughness can lead to a considerable decrease in the fatigue strength. In detail, Chan [35] has reported that the fatigue strength can be reduced by 60–75% due to surface notches resulting from the process-induced surface roughness. In prior studies, Masuo et al. [6] and Vayssette et al. [36] determined a fatigue strength of $\sigma_a = 200$ MPa and $\sigma_a = 240$ MPa for 10^5 cycles, respectively. Compared to the results presented, a slightly lower fatigue

strength (cf. Fig. 7) was determined. A possible explanation for this was recently delivered by Razavi et al. [37] investigating the effect of build thickness on the mechanical properties of PBF-EB-manufactured Ti6Al4V. It was reported that thinner specimens show a lower fatigue strength compared to bigger specimens whereby authors attributed this to the higher surface to volume ratio. In particular, the high ratio of micro-notch depth to the specimen cross section was highlighted as a detrimental factor. Based on the fractographic analysis (cf. Fig. 10), it was shown that the fatigue cracks initiated only at the specimens' surface due to local stress concentrations mainly resulting from notch-like defects. Thereby, the geometrical parameters of the notch-like defect determine its criticality. Furthermore, multiple crack initiation sites were present, thus, the exact fatigue crack origin at the most harmful defect is hard to state. As already mentioned above, the formation of notch-like defects results from non-optimal process parameters.

Regarding the influence of the position on the BP on the mechanical properties of PBF-EB-manufactured Ti6Al4V, only few studies are available. Galarraga et al. [20] have stated in their investigations that tensile properties are varying as a function of the position on the BP. In detail, specimens in the front of the BP show highest YS and UTS as well as fracture strain. On the contrary, specimens in the center of the BP were found to have the lowest values. Comparing this to the present results, no clear differentiation between different positions on the BP can be made; however, some tendencies are visible. As highlighted in Fig. 9a, specimens in the front of the BP show slightly weaker fatigue properties at higher stress amplitudes compared to the back of the BP. With decreasing stress amplitudes, these differences are reduced and might be negligible. Even for specimens which are located at the border of the BP, lower fatigue life compared to specimens in the center, independent of the stress amplitude, was detected. However, it has to be mentioned that subsequent tests with an increased number of specimens are needed in order to clearly determine the influence of different BP positions on the fatigue properties.

To improve the fatigue strength of the investigated alloy, subsequent post treatments are often carried out. It was already reported that solely a HIP treatment has a negligible effect on the fatigue life of specimens with as-built surface roughness [34]. A combination of surface finish and HIP was found to be the most effective way to improve the fatigue life of PBF-EB-manufactured Ti6Al4V [6, 24, 38]. Since relative density of the PBF-EB-manufactured parts is relatively high, it was stated by Fachhini et al. [13] that HIP leads to a slight increase in density but was not found to be the main reason for the improved fatigue life. The concurrent coarsening of the microstructure was rather found to inhibit the fatigue crack propagation leading to an increased fatigue life [10].

5 Conclusions

To transfer the PBF-EB process towards industrial applications, the process–structure–property relationships have to be understood in detail. Within this work, the defect and hardness distribution as well as the cyclic properties of the PBF-EB-manufactured Ti6Al4V alloy were investigated as a function of the position on the building platform. In particular, surface roughness was found to change for different locations on the building platform most likely due to the presence of partially melted powder particles on the surface as well as the individual formation of stacking defects resulting from the morphology of the material layer. Based on the μ-CT scans, an average surface roughness Ra = 41 μm was detected. However, only minor differences were detected for the relative density and the process-induced hardness. It could be demonstrated that all specimens are affected by an undersized effective diameter which has to be considered for the near-net-shape production. In particular, it was shown that the diameter changes even for single material layers leading to the formation of notch-like defects which were later found to be the preferred location of early crack initiation. With regard to known literature, comparable results could be determined within the fatigue tests whereby specimens in the front of the building platform show slightly lower fatigue performance compared to the back of the building platform. Even specimens located at the border show a lower fatigue life compared to the center. However, further investigations are needed with an increased number of specimens. Furthermore, surface quality might be improved to clearly examine the influence of the specimen position within the building platform on the mechanical properties.

Declarations

Conflict of interest The authors declare that they have no known competing financial interests or personal relationships that could have appeared to influence the work reported in this paper.

References

1. Liu S, Shin YC (2019) Additive manufacturing of Ti6Al4V alloy: a review. Mater Des 164:107552. https://doi.org/10.1016/j.matdes.2018.107552
2. Li P, Warner DH, Fatemi A, Phan N (2016) Critical assessment of the fatigue performance of additively manufactured Ti–6Al–4V and perspective for future research. Int J Fatigue 85:130–143. https://doi.org/10.1016/j.ijfatigue.2015.12.003
3. Murr LE, Gaytan SM, Medina F, Lopez H, Martinez E, Machado BI, Hernandez DH, Martinez L, Lopez MI, Wicker RB, Bracke J (2010) Next-generation biomedical implants using additive manufacturing of complex, cellular and functional mesh arrays. Philos Trans A Math Phys Eng Sci 368(1917):1999–2032. https://doi.org/10.1098/rsta.2010.0010
4. Reddy KS, Dufera S (2016) Additive manufacturing technologies. BEST: Int J Manag Inf Technol Eng 4(7): 89–112
5. Chastand V, Tezenas A, Cadoret Y, Quaegebeur P, Maia W, Charkaluk E (2016) Fatigue characterization of Titanium Ti-6Al-4V samples produced by additive manufacturing. Procedia Struct Integr 2:3168–3176. https://doi.org/10.1016/j.prostr.2016.06.395
6. Masuo H, Tanaka Y, Morokoshi S, Yagura H, Uchida T, Yamamoto Y, Murakami Y (2017) Effects of defects, surface roughness and HIP on fatigue strength of Ti-6Al-4V manufactured by additive manufacturing. Procedia Struct Integr 7:19–26. https://doi.org/10.1016/j.prostr.2017.11.055
7. Günther J, Krewerth D, Lippmann T, Leuders S, Tröster T, Weidner A, Biermann H, Niendorf T (2017) Fatigue life of additively manufactured Ti–6Al–4V in the very high cycle fatigue regime. Int J Fatigue 94:236–245. https://doi.org/10.1016/j.ijfatigue.2016.05.018
8. Edwards P, O'Conner A, Ramulu M (2013) Electron beam additive manufacturing of titanium components: properties and performance. J Manuf Sci Eng 135(6):525. https://doi.org/10.1115/1.4025773
9. Chern AH, Nandwana P, Yuan T, Kirka MM, Dehoff RR, Liaw PK, Duty CE (2019) A review on the fatigue behavior of Ti-6Al-4V fabricated by electron beam melting additive manufacturing. Int J Fatigue 119:173–184. https://doi.org/10.1016/j.ijfatigue.2018.09.022
10. Zhao X, Li S, Zhang M, Liu Y, Sercombe TB, Wang S, Hao Y, Yang R, Murr LE (2016) Comparison of the microstructures and mechanical properties of Ti–6Al–4V fabricated by selective laser melting and electron beam melting. Mater Des 95:21–31. https://doi.org/10.1016/j.matdes.2015.12.135
11. Zhai Y, Galarraga H, Lados DA (2016) Microstructure, static properties, and fatigue crack growth mechanisms in Ti-6Al-4V fabricated by additive manufacturing: LENS and EBM. Eng Fail Anal 69:3–14. https://doi.org/10.1016/j.engfailanal.2016.05.036
12. Seifi M, Salem A, Satko D, Shaffer J, Lewandowski JJ (2017) Defect distribution and microstructure heterogeneity effects on

fracture resistance and fatigue behavior of EBM Ti–6Al–4V. Int J Fatigue 94:263–287. https://doi.org/10.1016/j.ijfatigue.2016.06.001

13. Facchini L, Magalini E, Robotti P, Molinari A (2009) Microstructure and mechanical properties of Ti-6Al-4V produced by electron beam melting of pre-alloyed powders. Rapid Prototyp J 15(3):171–178. https://doi.org/10.1108/13552540910960262

14. Elambasseril J, Lu SL, Ning YP, Liu N, Wang J, Brandt M, Tang HP, Qian M (2019) 3D characterization of defects in deep-powder-bed manufactured Ti–6Al–4V and their influence on tensile properties. Mater Sci Eng A 761:138031. https://doi.org/10.1016/j.msea.2019.138031

15. Kotzem D, Ohlmeyer H, Walther F (2020) Damage tolerance evaluation of a unit cell plane based on electron beam powder bed fusion (E-PBF) manufactured Ti6Al4V alloy. Procedia Struct Integr 28:11–18. https://doi.org/10.1016/j.prostr.2020.10.003

16. Wang P, Sin WJ, Nai MLS, Wei J (2017) Effects of processing parameters on surface roughness of additive manufactured Ti-6Al-4V via electron beam melting. Materials (Basel). https://doi.org/10.3390/ma10101121

17. Hrabe N, Quinn T (2013) Effects of processing on microstructure and mechanical properties of a titanium alloy (Ti–6Al–4V) fabricated using electron beam melting (EBM), Part 2: energy input, orientation, and location. Mater Sci Eng A 573:271–277. https://doi.org/10.1016/j.msea.2013.02.065

18. Koike M, Greer P, Owen K, Lilly G, Murr LE, Gaytan SM, Martinez E, Okabe T (2011) Evaluation of titanium alloys fabricated using rapid prototyping technologies-electron beam melting and laser beam melting. Materials (Basel) 4(10):1776–1792. https://doi.org/10.3390/ma4101776

19. Persenot T, Martin G, Dendievel R, Buffiére J-Y, Maire E (2018) Enhancing the tensile properties of EBM as-built thin parts: Effect of HIP and chemical etching. Mater Char 143:82–93. https://doi.org/10.1016/j.matchar.2018.01.035

20. Galarraga H, Lados DA, Dehoff RR, Kirka MM, Nandwana P (2016) Effects of the microstructure and porosity on properties of Ti-6Al-4V ELI alloy fabricated by electron beam melting (EBM). Addit Manuf 10:47–57. https://doi.org/10.1016/j.addma.2016.02.003

21. Kotzem D, Dumke P, Sepehri P, Tenkamp J, Walther F (2019) Effect of miniaturization and surface roughness on the mechanical properties of the electron beam melted superalloy Inconel®718. Prog Addit Manuf 117:371. https://doi.org/10.1007/s40964-019-00101-w

22. Galarraga H, Warren RJ, Lados DA, Dehoff RR, Kirka MM, Nandwana P (2017) Effects of heat treatments on microstructure and properties of Ti-6Al-4V ELI alloy fabricated by electron beam melting (EBM). Mater Sci Eng A 685:417–428. https://doi.org/10.1016/j.msea.2017.01.019

23. Kotzem D, Arold T, Niendorf T, Walther F (2020) Influence of specimen position on the build platform on the mechanical properties of as-built direct aged electron beam melted Inconel 718 alloy. Mater Sci Eng A 772:138785. https://doi.org/10.1016/j.msea.2019.138785

24. Persenot T, Burr A, Martin G, Buffiere J-Y, Dendievel R, Maire E (2019) Effect of build orientation on the fatigue properties of as-built electron beam melted Ti-6Al-4V alloy. Int J Fatigue 118:65–76. https://doi.org/10.1016/j.ijfatigue.2018.08.006

25. Lhuissier P, de Formanoir C, Martin G, Dendievel R, Godet S (2016) Geometrical control of lattice structures produced by EBM through chemical etching: investigations at the scale of individual struts. Mater Des 110:485–493. https://doi.org/10.1016/j.matdes.2016.08.029

26. Persenot T, Buffiere J-Y, Maire E, Dendievel R, Martin G (2017) Fatigue properties of EBM as-built and chemically etched thin parts. Procedia Struct Integr 7:158–165. https://doi.org/10.1016/j.prostr.2017.11.073

27. Suard M, Martin G, Lhuissier P, Dendievel R, Vignat F, Blandin J-J, Villeneuve F (2015) Mechanical equivalent diameter of single struts for the stiffness prediction of lattice structures produced by Electron Beam Melting. Addit Manuf 8:124–131. https://doi.org/10.1016/j.addma.2015.10.002

28. Körner C, Bauereiß A, Attar E (2013) Fundamental consolidation mechanisms during selective beam melting of powders. Model Simul Mater Sci Eng 21(8):85011. https://doi.org/10.1088/0965-0393/21/8/085011

29. Siddique S, Walther F (2017) Fatigue and fracture reliability of additively manufactured Al-4047 and Ti-6Al-4V alloys for automotive and aerospace applications. In: Bajpai RP, Chandrasekhar U (eds) Innovative design and development practices in aerospace and automotive engineering: I-DAD, February 22–24, 2016. Springer, Singapore, pp 19–25

30. Dallago M, Fontanari V, Torresani E, Leoni M, Pederzolli C, Potrich C, Benedetti M (2018) Fatigue and biological properties of Ti-6Al-4V ELI cellular structures with variously arranged cubic cells made by selective laser melting. J Mech Behav Biomed Mater 78:381–394. https://doi.org/10.1016/j.jmbbm.2017.11.044

31. Hernández-Nava E, Smith CJ, Derguti F, Tammas-Williams S, Leonard F, Withers PJ, Todd I, Goodall R (2016) The effect of defects on the mechanical response of Ti-6Al-4V cubic lattice structures fabricated by electron beam melting. Acta Mater 108:279–292. https://doi.org/10.1016/j.actamat.2016.02.029

32. Ataee A, Li Y, Fraser D, Song G, Wen C (2018) Anisotropic Ti-6Al-4V gyroid scaffolds manufactured by electron beam melting (EBM) for bone implant applications. Mater Des 137:345–354. https://doi.org/10.1016/j.matdes.2017.10.040

33. Vo TH, Museau M, Vignat F, Villeneuve F, Ledoux Y, Ballu A (2018) Typology of geometrical defects in electron beam melting. Procedia CIRP 75:92–97. https://doi.org/10.1016/j.procir.2018.04.033

34. Kahlin M, Ansell H, Moverare JJ (2017) Fatigue behaviour of additive manufactured Ti6Al4V, with as-built surfaces, exposed to variable amplitude loading. Int J Fatigue 103:353–362. https://doi.org/10.1016/j.ijfatigue.2017.06.023

35. Chan KS (2015) Characterization and analysis of surface notches on Ti-alloy plates fabricated by additive manufacturing techniques. Surf Topogr Metrol Prop 3(4):44006. https://doi.org/10.1088/2051-672X/3/4/044006

36. Vayssette B, Saintier N, Brugger C, Elmay M, Pessard E (2018) Surface roughness of Ti-6Al-4V parts obtained by SLM and EBM: effect on the high cycle fatigue life. Procedia Eng 213:89–97. https://doi.org/10.1016/j.proeng.2018.02.010

37. Razavi S, van Hooreweder B, Berto F (2020) Effect of build thickness and geometry on quasi-static and fatigue behavior of Ti-6Al-4V produced by Electron Beam Melting. Addit Manuf 36:101426. https://doi.org/10.1016/j.addma.2020.101426

38. Hrabe N, Gnäupel-Herold T, Quinn T (2017) Fatigue properties of a titanium alloy (Ti–6Al–4V) fabricated via electron beam melting (EBM): Effects of internal defects and residual stress. Int J Fatigue 94:202–210. https://doi.org/10.1016/j.ijfatigue.2016.04.022